



# The role of node fillet, unit-cell size and strut orientation on the fatigue strength of Ti-6Al-4V lattice materials additively manufactured via laser powder bed fusion

M. Dallago<sup>a,\*</sup>, S. Raghavendra<sup>a</sup>, V. Luchin<sup>b</sup>, G. Zappini<sup>b</sup>, D. Pasini<sup>c</sup>, M. Benedetti<sup>a</sup>

<sup>a</sup> Department of Industrial Engineering, University of Trento, Trento, Italy

<sup>b</sup> Lincotek Additive Trento, Pergine Valsugana, Italy

<sup>c</sup> Department of Mechanical Engineering, McGill University, Montreal, Canada

## ARTICLE INFO

### Keywords:

Defects  
Fatigue  
Lattice materials  
Laser Powder Bed Fusion  
Additive Manufacturing

## ABSTRACT

Laser Powder Bed Fusion (L-PBF) provides ample freedom to fabricate lattice materials with tailored micro-architecture. Nevertheless, small-scale structures often suffer from a wide range of morphological defects, which impact the macro-scale mechanical properties. In this work, prominent morphological factors including geometric irregularities (surface notches and cross-section deviation), node geometry and printing direction are assessed for four batches of L-PBF Ti-6Al-4 V cubic lattice specimens, and their fatigue behavior compared. The results show that smoothing the strut fillets at their node remarkably improves the S-N curves and that the printing direction impacts both the fatigue strength and the failure behavior.

## 1. Introduction

Lattice materials typically feature a periodic porous architecture, which differs from that of traditional materials. Their properties are not only governed by the chemical composition of the constituent solid, but also by the topology and geometry of the unit cell [1,2]. Low density, superior thermal insulation, high impact response and other properties have contributed to make cellular materials attractive to the aerospace, biomedical, automotive and naval industry [2-6]. For instance, stress-shielding, one cause of orthopaedic implant failure, is mitigated if a low modulus lattice with tailored porosity gradients is integrated at the interface with the bone tissue [7-10]. These and other high-end applications require the attainment of a highly controlled architecture called to satisfy often strict and diverse design requirements. On this front, additive manufacturing (AM), a layer-by-layer process, has a clear advantage over traditional fabrication technologies [11,12]. Powder bed fusion (PBF) is a subset of AM whereby a heat source is used to consolidate material in powder form to create three-dimensional (3D) objects. When the heat source is a laser, the process is named Laser-based Powder Bed Fusion (L-PBF) [13,14].

Despite L-PBF has been so far successfully used to produce complex lattice architectures [12,15], the properties of the printed parts can deviate significantly from those predicted assuming an ideal geometry and homogeneous properties of the base material [16]. Indeed, the

manufacturing process markedly affects the microstructure of the base 3D printed material and as well as the lattice architecture with an outcome that impacts mechanical and biological performance [17,18]. The quality of as-built L-PBF parts is typically influenced by high cooling rates and preferential grain growth direction caused by directional heat flow, which leads to the formation of low ductility metastable phases and anisotropy, respectively [19-22]. Fast cooling is also responsible for the occurrence of residual stresses that, besides altering the mechanical properties, can also cause distortions in the lattice [18,23]. Pores can be often found in L-PBF parts, which can be spherical or irregularly shaped [24].

The as-built architecture of a lattice material, on the other hand, can feature several types of geometrical defects and irregularities [5,25-30]. Partially unmelted particles increase the surface roughness [17]. On a larger scale, the size of the melt pool significantly affects the geometry of the lattice, e.g. strut thickness, strut straightness, junction alignment and junction shape [23,29,31]. The melt pool extent is determined by the input energy of the scanning laser and by the local heat transfer properties of the solid/powder system [27,32,33]. While the input energy, expressed by the specific energy, depends on the machine parameters [24], the local thermal properties can be ascribed mainly to the spatial orientation of the solidified material, the solid/powder fraction and the packing density of the powder [27,34]. Being the powder less conductive than solid, a larger melt pool is prompted to form in regions

\* Corresponding author.

E-mail address: [michele.dallago@unitn.it](mailto:michele.dallago@unitn.it) (M. Dallago).

<https://doi.org/10.1016/j.ijfatigue.2020.105946>

Received 22 June 2020; Received in revised form 6 September 2020; Accepted 8 September 2020

Available online 11 September 2020

0142-1123/ © 2020 Elsevier Ltd. All rights reserved.

supported prevalently or entirely by powder [27,28,34], leading to an accumulation of the solid material on the overhanging parts of the lattice [35,36]. Therefore, increasing the inclination angle of the struts to the build plane leads to a gradual decrease of the deviation from the nominal shape because the fraction of the melt pool supported by solid material grows [29,37]. On the other hand, inclined struts can be affected by the staircase effect, which is the outcome of the consecutive stacking of discrete layers welded together with a small offset due to inclination [34,38]. The complexity of the as-built/as-designed deviation is also amplified by solidification and cooling shrinkage [39].

In general, the mechanical performance of a lattice material is negatively affected by manufacturing defects, although the extent of such impact is highly variable. For instance, struts aligned with the direction of the applied load carry a higher fraction of the load and hence defects appearing on these struts have a major impact on the mechanical properties [17]. On the other hand, lattice materials suffer from an ample scatter in mechanical performance [40,41].

The effect of manufacturing defects on the quasi-static mechanical properties (elastic moduli and strength) has been addressed by several studies [23,30,32,42,43]. A decrease of struts straightness (waviness) and node displacement causes a loss of stiffness and strength due to the rise of bending actions, particularly in stretching dominated lattices. Any deviations of the cross-section shape and size from the nominal geometry alter the load bearing area, e.g. the second moment of area, of a strut, possibly increasing or decreasing the modulus. Although to a lesser degree compared to the other morphological defects, internal porosity and surface roughness decrease the elastic modulus [40]. Conversely, these factors have a stronger effect on the yield stress and the ultimate tensile strength because they act as stress raisers, inducing premature plasticization and subsequent rupture [17,40]. The relationship between build orientation of the struts and the manufacturing defects translates to a measurable effect on the mechanical properties of L-PBF lattices: the smaller the angle between the strut and the build plane, the lower is the strength [21]. A similar behavior was observed also in single struts [19].

In contrast to the elastic modulus and other monotonic properties, fatigue, a highly localized phenomenon, is very sensitive to the microstructural and morphological quality of a component, and thus it is extremely sensitive to the manufacturing process [44]. For example, the low fatigue strength of as-built L-PBF parts compared to machined or wrought parts is partly determined by the microstructure (less ductile), but even more by surface roughness [45,46]. Similarly, the fatigue behavior of L-PBF lattices is negatively impacted by surface defects, such as semi-molten powder particles, as well as by irregularities in the strut cross-sections that act as notches [23,47–49]. Furthermore, any geometric deviation that alters the stress distribution in the strut, such as geometric defects at the junction, acts as stress raiser [50,51]. These imperfections have a detrimental impact on the fatigue properties. Fatigue cracks typically nucleate on the surface in proximity of defects and much less within the bulk of the solid, where internal cavities in L-PBF parts often appear [49,52]. Ti-alloys, such as Ti-6Al-4 V, are especially sensitive to stress raisers due their high notch sensitivity [53,54]. Besides stress raiser, residual stress also contributes to the fatigue behavior [46,47,55].

This work examines the fatigue response of Ti-6Al-4 V regular cubic lattices 3D printed via L-PBF. In particular, the focus is on the fully-reversed fatigue S-N curves with the goal of investigating the role of the lattice orientation to the printing direction, junction geometry and unit cell size. We use a combination of optical microscopy, electron microscopy and fatigue testing to examine four batches of 3D printed specimens each with selected inclination ( $0^\circ$  versus  $90^\circ$ ) to the build plane, junction geometry (wide fillet versus sharp fillet), and unit cell sizes (3 mm and 4 mm).

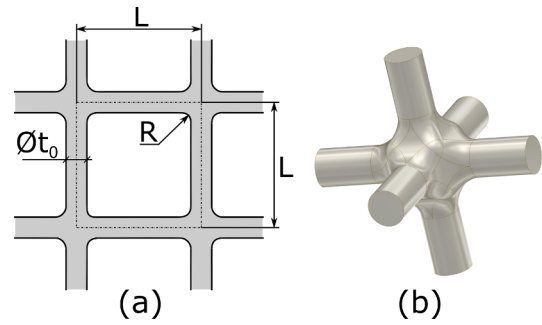


Fig. 1. Unit cell geometry: (a) parameter definition of in-plane geometry; (b) 3D view of unit cell.

## 2. Materials and methods

### 2.1. Specimen design and description

The unit cell examined in this work has a regular cubic topology of strut length  $L$  and strut diameter  $t_0$ . At the junctions, the struts are joined by circular arc fillets of in-plane radius  $R$  (Fig. 1a). The rationale behind the choice of the cubic unit cell is its simplicity which translates into an easy-to-control relationship between the printing direction and the loading direction of the struts and the possibility of obtaining well-defined fillet radii at the strut junctions. The results here obtained can be transferred to more complex topologies, thus providing insight into the fatigue design of lattice materials.

The lattice specimens were 3D printed via L-PBF using a Renishaw machine equipped with a pulsed laser with a nominal power of 200 W and starting from a spherical biomedical grade Ti6Al4V ( $O_2 < 0.2\%$ ) powder with a particle size in the range 15–45  $\mu\text{m}$ . A layer thickness of 60  $\mu\text{m}$  was deposited at each step. After fabrication, all specimens were subjected to a heat treatment in vacuum at Lincotek Additive Trento (Pergine Valsugana, Italy) at temperature above 800  $^\circ\text{C}$ , which lies in the  $\alpha + \beta$  bi-phasic field. The treatment is known to be sufficient in order to relieve residual stresses generated during the powder bed fusion process and to transform the martensitic as-built microstructure into a stable  $\alpha + \beta$  one [56]. Neither sandblasting nor other surface treatments were applied. To reduce the border effects to a reasonable level, the specimens were designed according to the guidelines provided by the ISO14333 standard: the cellular part is cylindrical, made of 12 unit cells along the height and 11 along the diameter (Fig. 2a and 2b). During half of the fully reversed fatigue cycle the specimen is in traction, therefore the specimen must be appropriately connected to the testing machine, a condition ensured by adding bolted flanges directly printed with the specimen. To indicate the printing orientation of the

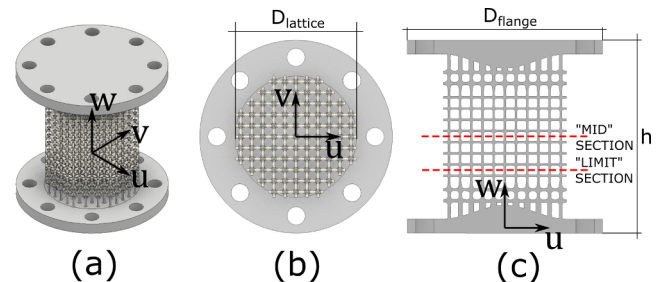
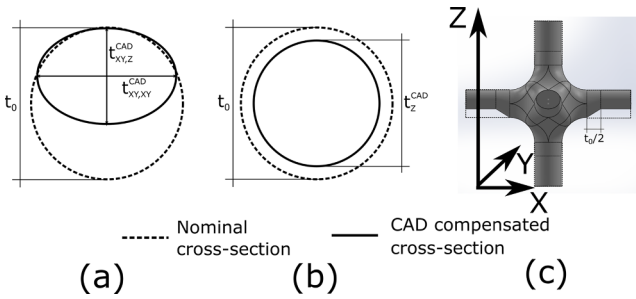


Fig. 2. Representative cellular specimen used for mechanical testing: (a) 3D view of the entire specimen, with  $uvw$  reference system; (b) view of specimen cross-section; (c) specimen longitudinal section, showing transition regions. i.e. bell shape and thicker struts close to the flange, between solid flanges and inner cellular portion.



**Fig. 3.** The compensation concept: the CAD strut cross-section parameters for a horizontal,  $t_{xy,z}^{CAD}$  (thickness along the Z direction) and  $t_{xy,xy}^{CAD}$  (thickness in the XY build plane), (a) and for a vertical strut,  $t_z^{CAD}$ , (b) are designed with the aid of the compensation model to produce the desired ( $t_0$ ) cross-section after manufacturing; (c) compensated CAD of the unit cell. Z-direction corresponds to the building direction while (X, Y) directions define the building plane.

specimen an XYZ reference system is used: the printing direction is indicated by Z, while the build plane is the XY plane.

The as-built/as-designed mismatch issue in L-PBF lattices can be addressed via a procedure known as compensation [29]. Such procedure proposes a design compensation of the currently inevitable manufacturing deviations in geometry, with the potential of using different levels of compensation for struts at dissimilar angles in the lattice. This paper mainly examines the relationship between the as-built geometric features and the fatigue behavior of lattice specimens with compensated geometry.

Compensation is based on the availability of mathematical relationships that tie the as-built geometry (minor and major axis of the elliptical cross-section) to the as-designed geometry (strut diameter  $t_0$ ). These expressions are then inverted, so that the parameters of the CAD cross-section ( $t_{xy,z}^{CAD}$ ,  $t_{xy,xy}^{CAD}$  and  $t_z^{CAD}$ ) that lead to the desired (nominal) circular cross-section (diameter  $t_0$ ) are obtained (Fig. 3a and 3b). Two expressions are needed for struts at low angles to the printing plane, while close-to-vertical struts typically retain their circular cross-section, hence one expression is sufficient. The compensated geometric parameters, considering the orientation of the struts to the printing direction, are used to draw the geometry of the regular cubic cell that repeated in space generates the CAD of the lattice (Fig. 3c). This compensated CAD model, fed to the L-PBF printer, allows to obtain an as-built lattice matching the nominal geometry. In this work, we use the expressions derived experimentally in a previous work [31] for lattices of the same type and printed with the same process parameters.

Four groups of specimens were examined, each identified by a capital letter (Fig. 4):

- Compensated specimens. The specimens are placed on the printer baseplate so as to align the printing direction to the loading direction (placed vertically).
- Compensated specimens identical to case A (compensation and filleted junctions), but printed with loading direction normal to printing direction (placed horizontally).
- Compensated specimens as in A, but without fillets at the nodes.
- Compensated specimens as in A, but with smaller unit cell size  $L$  and scaled  $R$  and  $t_0$ .

For each group, eight specimens were manufactured. Batches from A to D were designed with the parameters of the nominal geometry listed in Table 1 ( $L = 4000 \mu\text{m}$ ,  $t_0 = 670 \mu\text{m}$ ,  $R = 600 \mu\text{m}$ ); for batch E the unit cell size  $L$  is  $3000 \mu\text{m}$ , and the  $t_0/L$  and  $R/L$  ratios are identical to the other batches, hence  $t_0 = 500 \mu\text{m}$  and  $R = 450 \mu\text{m}$ . The nominal geometry of the specimens was determined with the procedure described in a previous work [48], requesting the nominal elastic modulus to be 3 GPa. Table 1 summarizes nominal and compensated parameters of the cell geometry.

Table 2 lists the size of the specimens (parameters in Fig. 2), which depends on the unit cell size  $L$ .

To guarantee the validity of the fatigue tests, two requirements should be met: failure should occur away from the flanges and the internal load distribution should be uniform within the cross-section of the cellular specimen. These conditions are not trivial to fulfill, given the geometric characteristics of the specimen, which is cellular as opposed to the standard sample of solid material. Fig. 5 shows the computational result of an iterative design process using FE (Ansys® Release 18.0) models of the specimens including the bolts. The specimen was generated with nominal values of the geometrical parameters and meshed with 10 node tetrahedral structural elements (SOLID187) and simulated in tension. In this article only a brief description of the design process is given, while a more detailed account of the procedure is planned for a future publication.

The strategy devised to avoid failure close to the flanges consists of thickening both the vertical struts and fillets of the unit cells in the planes interfacing the flanges. The compliance of the flange causes the external annulus of the cellular specimen to carry a higher fraction of the load, unless the thickness of the flange is increased at its center. The simplest expedient was to design the flange shaped as a bell (Fig. 2c). Fig. 5 shows a plot of the normalized load in the struts (defined as the ratio between the force calculated from the FE simulations and the force calculated as if the traction was carried uniformly by all the struts) for two sections along the  $w$  axis of the specimen (see Fig. 2c). The results confirm that an increase of the flange thickness at its center improves the load distribution so as to make it more uniform. The difference in loading between the center and the external annulus decreases from

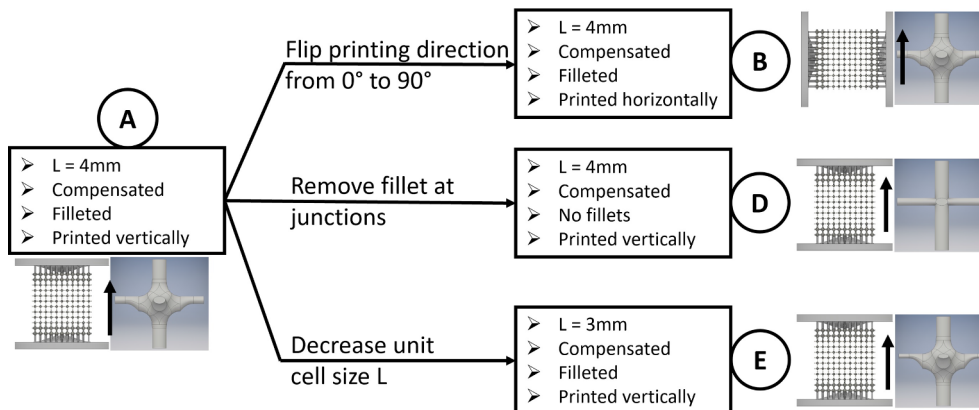


**Fig. 4.** Scheme showing the differences between the five batches of specimens used in the fatigue tests. The black arrows indicate the printing direction Z.

**Table 1**

Nominal and compensated geometrical parameters of the batches designed for mechanical testing.

Batch ID	Nominal (desired) geometry				Compensated CAD parameters		
	$R(\mu\text{m})$	$t_0(\mu\text{m})$	$L(\mu\text{m})$	Relative density (%)	$t_z^{\text{CAD}}(\mu\text{m})$	$t_{xy,z}^{\text{CAD}}(\mu\text{m})$	$t_{xy,xy}^{\text{CAD}}(\mu\text{m})$
A	600	670	4000	7.34	636	476	550
B	600	670	4000	7.34	636	476	550
D	0	670	4000	5.94	636	476	550
E	450	500	3000	7.27	480	300	377

**Table 2**

Specimens size of designed for mechanical testing (as defined in Fig. 2).

Specimen ID	h (mm)	$D_{\text{flange}}$ (mm)	$D_{\text{lattice}}$ (mm)
A – B – D	69	70	44
E	58	59	33

roughly 30% to 10%. This difference further increases if no transition zone is added between the solid flange and the cellular sample, leading to failure in the external annulus, at the region attached to the flange.

## 2.2. Experimental methods

### 2.2.1. Metrological characterization

For the metrological characterization of the specimens, we adopt a procedure previously developed [31]. Four specimens were randomly selected from each batch, and the Nikon SMZ25 stereomicroscope was used to take photographs of 8–12 unit cells along the directions perpendicular and parallel to the printing direction. Specimens of type A, D and E had to be cut in the  $uv$  plane of the specimen (Fig. 2a) to obtain pictures perpendicular to the printing direction. The mean value and

the standard deviation of the geometrical parameters for each batch are calculated using all the measurements obtained from the different pictures.

### 2.2.2. Microstructure

Metallographic specimens were prepared to investigate the microstructure and assess the effect of the heat treatment. For each batch, two specimens were prepared, one parallel and one perpendicular to the printing direction. The sectioned samples were then mounted, ground with SiC abrasive papers (with 120, 180, 320, 400, 600, 1000, 1500 grit sizes), and polished with a 3- $\mu\text{m}$  diamond paste followed by a 1- $\mu\text{m}$  paste. A Kroll's etching was finally applied to reveal the microstructures.

### 2.2.3. Micro-hardness

Microhardness values were measured to offer a means of comparison of the mechanical properties of the bulk material between the batches. A diamond Vickers indenter was used to apply a maximum force of 1 N. The load was applied at a constant 0.1 N/s rate with a dwell time of 10 s. Six measurements were performed on a parallel and a perpendicular section to the printing direction for a specimen of each batch.

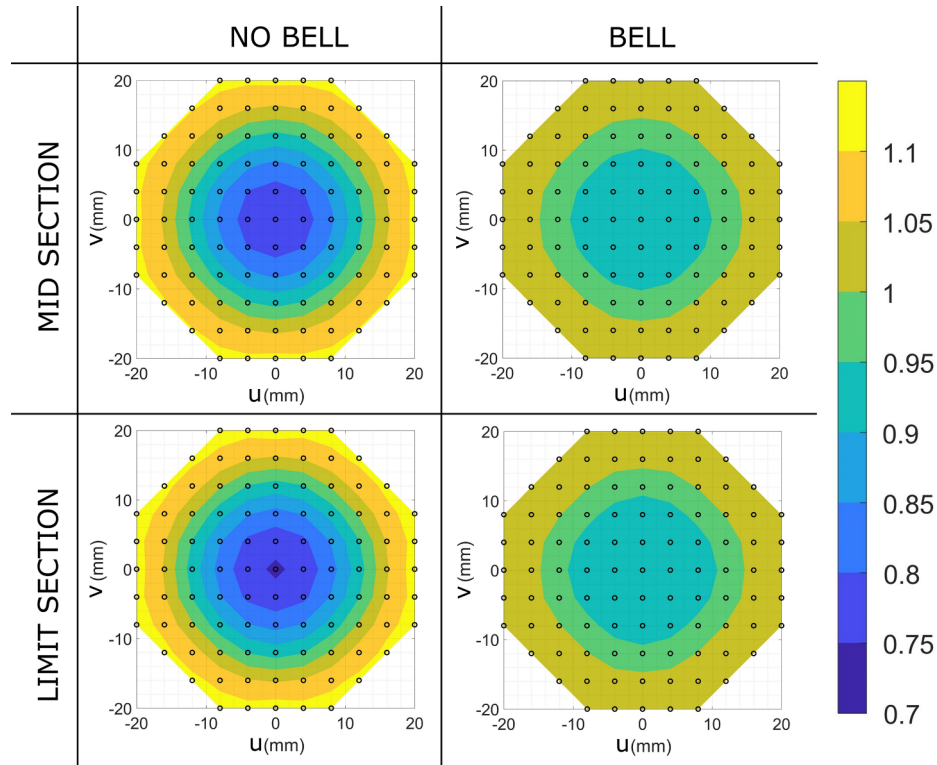


**Fig. 5.** Normalized load distribution in the “mid” and in the “limit” sections (see Fig. 13c) of the specimen with and without bell shape and thickness increase of the pillars. Small black circles represent strut locations.



#### 2.2.4. FE simulations

A set of numerical simulations were carried out to assess the lattice responses in the linear regime only using Ansys® Mechanical APDL, Release 18.0 (Canonsburg, Pennsylvania, U.S.A). A reduced model consisting of one unit cell (Fig. 1b and, after meshing with 3D 20 node structural continuum elements, Fig. 6) for both the nominal geometry and the as-built geometry was developed with results later compared with their experimental counterparts. For the base material (bulk Ti-6Al-4 V), we use the following properties: elastic modulus of 113 GPa and Poisson's ratio of 0.34. The FE models were used to calculate the fatigue notch factor  $K_f^*$  at the filleted joints defined assuming a worst-case scenario of notch sensitivity  $q = 1$  (full notch sensitivity) [23]:

$$K_f^* = K_t^* = \frac{\text{maximum principal stress at the joint}}{\text{nominal homogeneous stress}} \quad (1)$$

Where the nominal homogeneous stress is the ratio between the load on the unit cell and the nominal area of the unit cell ( $L \times L$ ). The maximum principal stress was deemed more appropriate than the von Mises equivalent stress because of the likely presence of a brittle alpha phase on the surface of the lattice [23].

FE models with the following characteristics were devised:

- unit cell with nominal geometrical parameters of batch A ( $L = 4$  mm,  $t_0 = 0.670$  mm,  $R = 0.600$  mm)
- unit cell with nominal geometrical parameters of batch E ( $L = 3$  mm,  $t_0 = 0.500$  mm,  $R = 0.450$  mm)
- unit cell with average as-built geometrical parameters measured in batch A ( $L = 4$  mm,  $t_z^{ab} = 0.693$  mm,  $R = 0.318$  mm)
- unit cell with average as-built geometrical parameters measured in batch D ( $L = 4$  mm,  $t_z^{ab} = 0.698$  mm,  $R = 0.090$  mm)
- unit cell with average as-built geometrical parameters measured in batch E ( $L = 3$  mm,  $t_z^{ab} = 0.527$  mm,  $R = 0.442$  mm)

The as-built geometrical parameters are listed in the Appendix and discussed in Paragraph 3.3.1. In the models representing the as-built unit cell, the fillet radius is equal to the smallest value among the average values of the three categories in which the measured radii are classified ( $R_+$ ,  $R_-$  and  $R_{lat}$ , as defined in Fig. 9). The diameter of the struts is the average diameter of the struts aligned with the loading direction (in all cases  $t_z^{ab}$ , as in Fig. 8). Solving the FE model for the nominal geometry of batch B is not needed because it is the same of batch A. On the other hand, since failure occurs in the struts and not at the junction, modelling the as-built geometry of batch B requires a more accurate approach which is left for future work.

A convergence study was performed for each FE model by refining the mesh and calculating the error on the maximum principal stress for each level of mesh refinement with respect to the finest one. The results were deemed to have converged satisfactorily when the error was equal or below 1%.

#### 2.2.5. Compression testing

An Instron 8516 testing machine was used for quasi-static compressive tests of cellular specimens, equipped with a 100 kN load cell (nonlinearity  $\pm 0.1\%$  of R.O.) and an axial extensometer (25 mm gauge length for batches A to D and 12.5 for batch E). The crosshead speed was 1 mm/min. The elastic modulus was measured by calculating the slope of loading-unloading cycles according to ISO 13314. This is necessary because both in compression and tension the slope of the first portion (the elastic part) of the stress-strain curve is lower than that of the successive unloading-loading curves due to local plastic effects [57]. A destructive monotonic compression test was carried out to estimate the 0.2% offset stress and the peak stress (first maximum compressive strength).

Only one specimen per batch was tested and the authors recognize that this choice does affect the reliability of the results of the

compression test, considering also the well-known scatter that affects the mechanical properties of L-PBF cellular lattices. Nevertheless, we still deem these results offer a qualitative comparison between the batches. Moreover, the 0.2% offset compression stress is used to normalize the S-N curves, allowing the comparison with results obtained previously.

#### 2.2.6. Fatigue testing

S-N curves were built using seven specimens per batch, subjected to fully reversed fatigue cycles ( $R = -1$ ) on a Rumul 50 kN Testronic resonant testing machine equipped with a 50 kN load cell under load control, at 120 Hz. Each specimen was considered failed if the resonant frequency decreased of 1 Hz, which corresponds to the complete failure of a few struts (4–5). Proceeding with the test would lead to complete specimen failure after a few hundred cycles. Subsequently, the specimen was completely broken by applying a monotonic static tension to identify the crack origin. Runout specimens were tested again at a load at least 1.5 times higher than the runout load to obtain additional data points. The S-N curve of the base material was also constructed using 12 fully dense specimens (gauge section diameter and length of 4 mm and 12 mm, respectively) printed along their loading direction with same machine parameters and powder as the cellular specimens, tested under identical loading conditions.

The data on fatigue are fitted with an asymptotic curve, given by:

$$\sigma_a = c_1 + \frac{c_2}{N_f^m} \quad (2a)$$

where  $\sigma_a$  is the homogeneous axial stress amplitude (the ratio between the load on the unit cell and the nominal circular area of diameter  $D_{lattice}$  of the lattice part, as in Fig. 2 and Table 2),  $N_f$  is the number of cycles to failure and the remaining quantities are fitting constants. The scatter of the fatigue data is assessed by computing the estimated regression variance assumed to be uniform for the whole fatigue life range and expressed by:

$$S^2 = \frac{\sum_{i=1}^n (\sigma_{a,i} - \hat{\sigma}_{a,i})^2}{n - p} \quad (2b)$$

where  $\sigma_{a,i}$  is the  $i$ .th fatigue amplitude data point,  $\hat{\sigma}_{a,i}$  is its estimator,  $n$  is the number of data elements, and  $p$  is the number of parameters in the regression ( $p = 3$  in this specific case).

The fatigue notch factor  $K_f^*$  was calculated from the experimental fatigue results by dividing the fatigue strength of the fully dense specimens and by the fatigue strength of the cellular specimens normalized by the nominal cross-section area of the specimen.

To distinguish the struts failed by fatigue from those failed by static tension, the fracture surfaces were investigated under a JEOL JSM-IT300LV scanning electron microscope (SEM).

### 2.3. Results and discussion

#### 2.3.1. Metrological characterization

Fig. 7 shows optical micrographs representative of the morphology of each batch. The nominal lattice is overlaid to compare the as-built and the as-designed architecture. Although the compensation leads to a satisfactory correspondence between the as-built and the as-designed lattice, the horizontal struts (parallel to the printing plane) are more irregular than the vertical struts in all the batches (as also indicated by the wider error bars on  $t_{xy,z}^{ab}$  and  $t_{xy,xy}^{ab}$  in Fig. 8). In Fig. 7A, for instance, the horizontal strut on the bottom is considerably thinner in the middle than towards the junction. This is a well-known phenomenon in overhanging PBF parts which are supported prevalently by the powder and not solid material. Where planned, the filleted junctions were reproduced satisfactorily, although the fillets on the underside of the horizontal struts seem more irregular than those above the struts. On the other hand, it is quite striking the sharpness of the junctions in

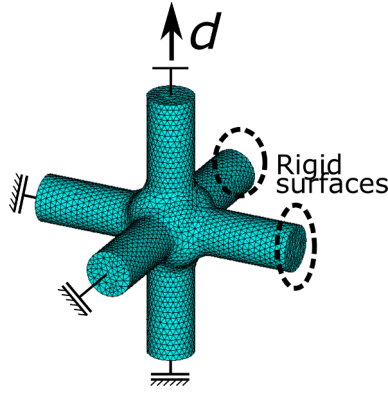


**Fig. 6.** Example of FE mesh of the unit cell and boundary conditions used to calculate the notch factor.  $d$  is a unitary displacement.

batch D, compared to the other specimens. The strategy to upscale the lattices compared to previous works [23,48] shows a clear improvement in the morphological quality of the junction (compare with Fig. 7 [24]).

For a systematic data representation, we classify the fillets into three categories defined according to the location of the fillet with respect to the struts meeting at the joint using the printing direction as a reference. A fillet is defined positive if its position is above the strut ( $R_+$ ), negative if it is below the strut ( $R_-$ ), and lateral if it lays in the plane normal to the printing direction ( $R_{lat}$ ), as shown in the drawing of Fig. 9. The fillets above the struts oriented at  $0^\circ$  are very close to the nominal value, whereas those below are sharper than in the other locations of the lattice, suggesting the presence of a systematic weak spot for fatigue resistance. The morphological differences between batches with filleted junctions are not significant. On the other hand, as expected the as-built fillet radii of batch D are very sharp, roughly  $100\ \mu\text{m}$ .

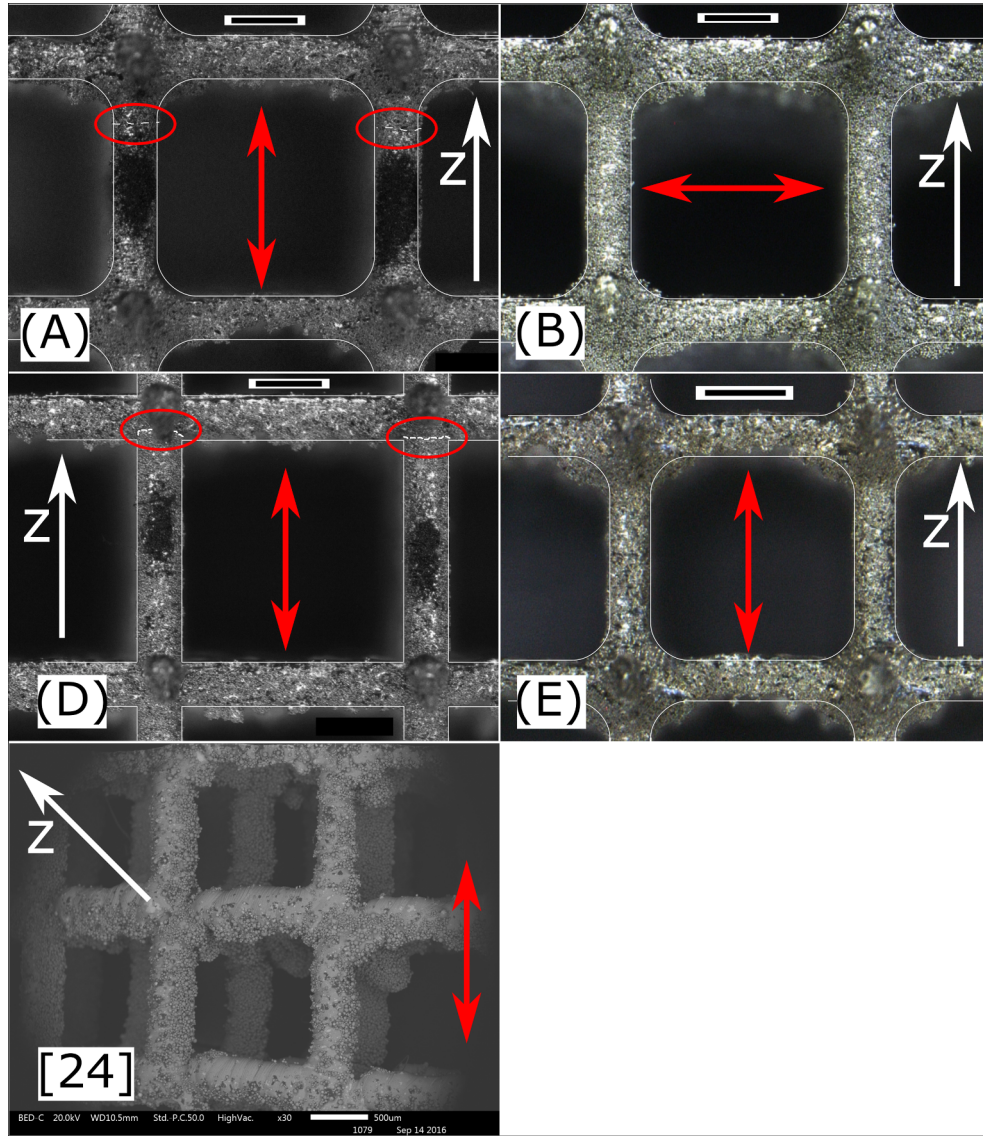


**Fig. 7.** Detail of a specimen from batch A (compensated and with filleted junctions), a specimen from batch B (compensated and with filleted junctions), a specimen from batch D (compensated and without filleted junctions) and a specimen from batch E (as A, but unit cell size 3 mm). Compare with the regular cubic lattices fabricated in [23] ( $L = 1.5\ \text{mm}$ ,  $t_0 = 0.230\ \text{mm}$ ,  $R = 0.130\ \text{mm}$ ). White arrows indicate printing direction, whereas the red double arrows the load direction. The white dashed lines (in (A) and (D), enclosed in red circles indicate where the struts failed by fatigue. The scale bars are all 1 mm for (A) to (E).



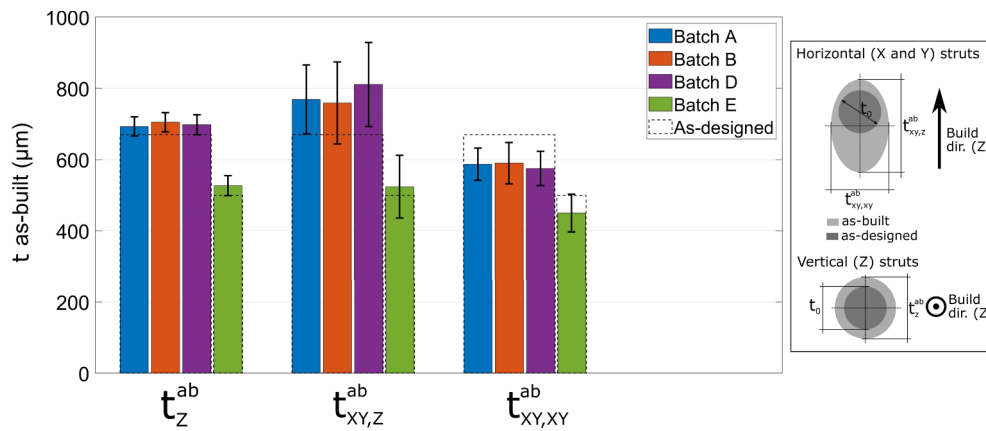


**Fig. 8.** As-built strut cross-section parameters with standard deviation classified according to the inclination of the struts to the printing plane. The dashed bars indicate the as-designed value of the strut diameter (670  $\mu\text{m}$  for batches A to D and 500  $\mu\text{m}$  for batch E). In the Appendix (Table A1), the numerical values are listed.

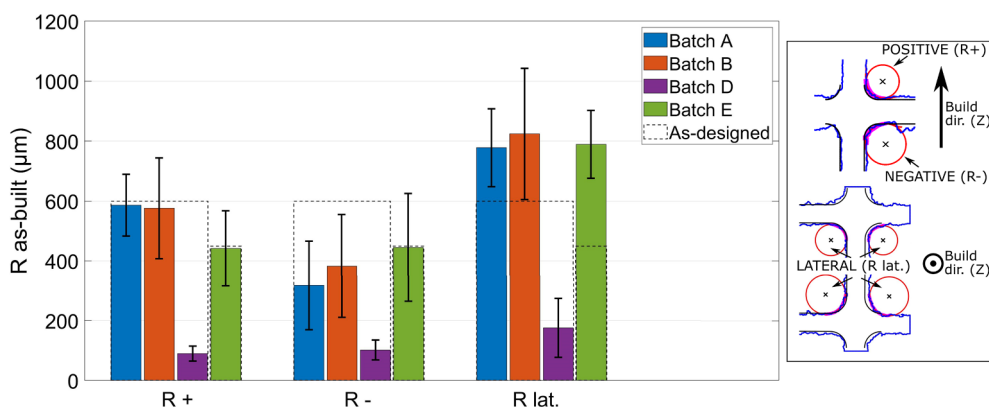


**Fig. 9.** As-built fillet radius with standard deviation measured in the various locations of the lattice. “R<sub>+</sub>” and “R<sub>-</sub>” represent the positive and the negative radius, respectively. “R<sub>lat</sub>” refers to the fillets measured in the build plane. The dashed line indicates the as-designed radius (600  $\mu\text{m}$  for batches A to D and 450  $\mu\text{m}$  for batch E). In the Appendix (Table A2), the numerical values are listed.

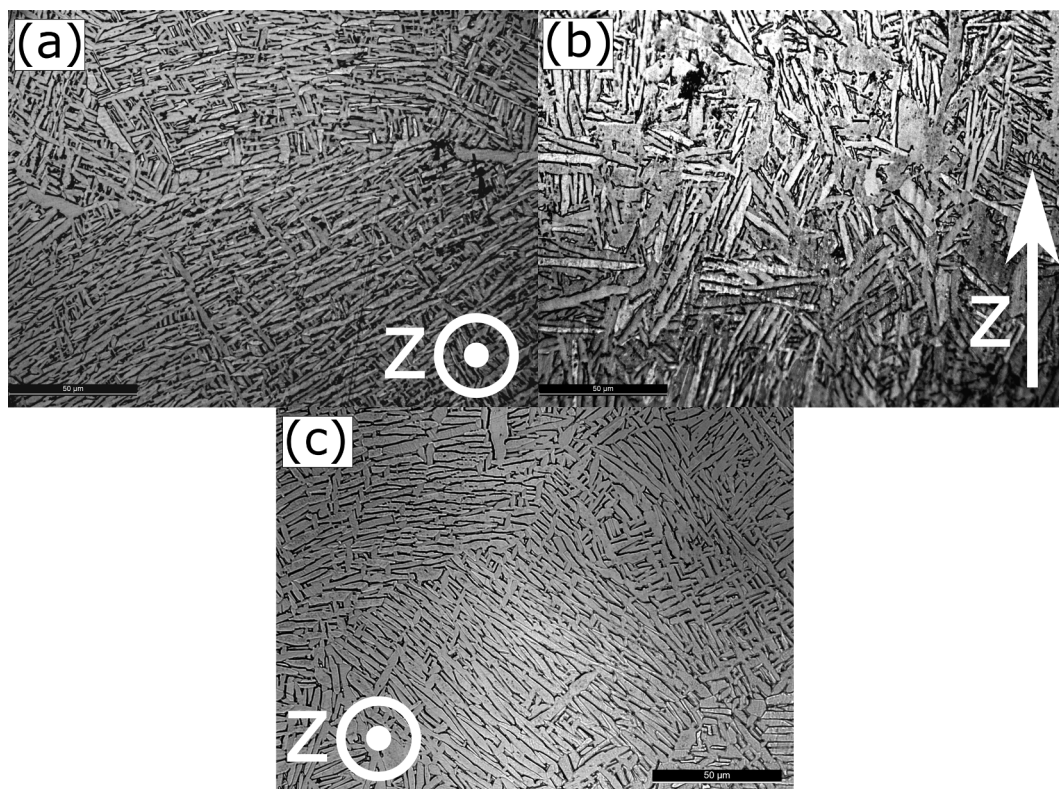


**Fig. 10.** The microstructure after the stress relief heat treatment is  $\alpha + \beta$  (white  $\alpha$  lamellae in a black  $\beta$  matrix): (a) section perpendicular to the printing direction (XY plane); (b) section parallel to the printing direction (YZ plane); (c) XY section of the fully dense specimens. The arrows indicate the printing direction.

**Table 3**

Microhardness values for each batch compared with bulk L-PBF bulk Ti6Al4V specimens printed with the same process parameters.

Bulk specimens	A	B	D	E
348 ± 15	354 ± 13	340 ± 20	347 ± 11	334 ± 20

**Table 4**

Elastic modulus (calculated from the loading–unloading tests), 0.2% offset stress and peak stress (monotonic tests) for each batch.

	A	B	D	E
Elastic modulus[MPa]	3021	1749	1844	2984
0.2% offset stress[MPa]	16	9	9	14
Peak stress[MPa]	16	9	9	15

As a final note on this matter, it was observed that the specimens printed horizontally (batch B) show a slight overall curvature out of the printing plane that is not observed in the specimens printed vertically. This curvature most likely is detrimental to the mechanical properties because it causes the rise of bending actions in struts that otherwise should be loaded by pure compression.

### 2.3.2. Microstructure

Fig. 10 shows that the microstructure of the Ti6Al4V specimen here characterized is a coarse lamellar  $\alpha + \beta$ , where the  $\alpha$  lamellae (light colored phase) are embedded in a  $\beta$  matrix (dark phase). This microstructure is obtained after heat treatment able to transform the strong but brittle fine acicular martensitic microstructure obtained after L-PBF into the more ductile equilibrium  $\alpha + \beta$  microstructure. The microstructure of the fully dense specimens fatigue specimens, manufactured and tested under same conditions as the lattice specimens, is shown for comparison (Fig. 10c).

### 2.3.3. Micro-hardness

There are no significant differences in the micro-hardness values among the batches (Table 3). Moreover, the results are also comparable with the measurements carried out on Ti6Al4V bulk specimens manufactured with the same process parameters. This result shows that using the bulk material properties in the FE models of the lattice materials is an acceptable approach. On the other hand, the effect of the surface, internal porosity and printing direction can have a different effect on the small struts of the lattice than on the larger bulk specimens. To clarify this aspect further testing is necessary, using miniature tensile specimens that represent single struts. This is left for future work.

### 2.3.4. Compression testing

The nominal value of the elastic modulus is 3 GPa and it is matched only by batches A and E (Table 4). On the other hand, the specimens printed horizontally have very low elastic modulus. Although it might be difficult to speculate on this result given the small number of specimens involved, the low elastic modulus of the specimens printed horizontally can be most likely ascribed to the high irregularity of the struts and possibly to the overall slight curvature of the specimens, introducing a spurious bending action that significantly lowers the global stiffness of the sample.

The 0.2% offset stress and the peak stress values calculated from the monotonic loading curves (Table 4 and Fig. 11) show that batches A and E perform very similarly, as expected from the design. No size effect is observed. Struts with low junction stiffness (batch D) are more prone to early failures and this can be explained by considering that the cubic lattice is stretching dominated under compression and it fails by buckling. The low peak stress of batch B, in which the load bearing struts were printed horizontally, is most likely related to the intrinsically weaker horizontal struts.

### 2.3.5. Fatigue testing

In this section, we discuss the effect of the junction geometry, the printing direction, and the unit cell size on the absolute and normalized S-N curves. The analysis of the correlation of the fatigue failure behavior with the lattice geometry is examined through the analysis of the failure zones (struts or junctions) and fracture surfaces obtained via optical and electron microscopy. The notch-like behavior of the junctions is also discussed with the support of FE simulations.

The comparison of the S-N curves obtained from the fatigue tests of batches A (filleted junctions) and D (non-filleted junctions) illustrates the effect of introducing round fillets at the strut junctions. In Fig. 12a it can be seen that filleted junctions remarkably increase the fatigue strength (in this case of a factor of 2 at  $10^6$  cycles). Batch E is not significantly different from batch A as expected from nominal CAD geometry: the nominal relative densities are respectively 7.27% and 7.34% (see also Table 1) and the nominal stress concentration factor (as per FE calculations) is 63 for both (see Table 5). It is interesting to note that in the batches printed along their loading direction (A, D and E) the struts fail very close to the junction, as it would be expected if failure would correlate to the stress concentration factor caused by the change in curvature at the fillet (Fig. 13A). Moreover, it was observed that the fatigue fracture always occurred in the part of the junction below the horizontal struts (using the printing direction as a reference), at the fillets identified with “R-“ (see definition in Fig. 9). This is also shown in Fig. 7A and 7D, where the first struts to fail during fatigue testing, belonging to specimens from batch A and D respectively, show the

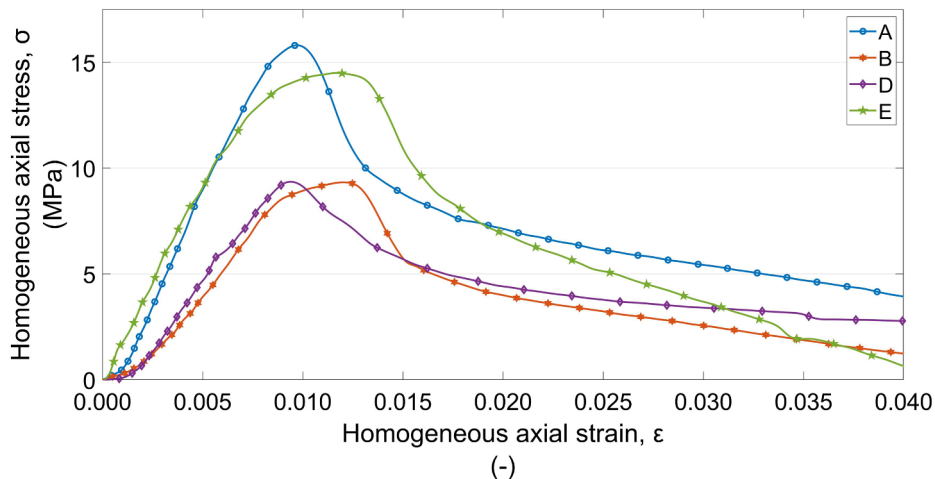
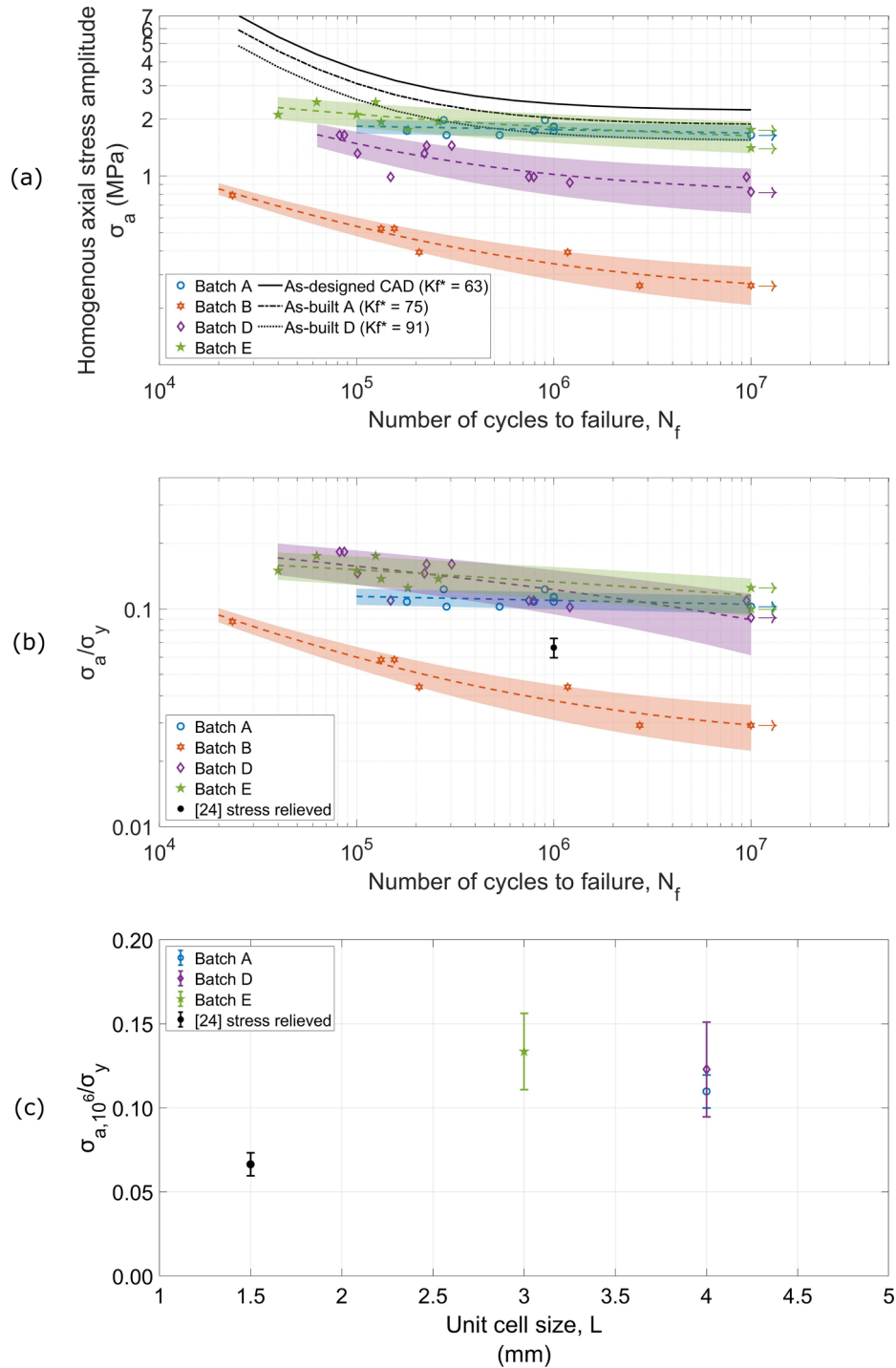


Fig. 11. Monotonic compressive stress–strain curves. The stress is normalized by the nominal cross-section of the specimen.





**Fig. 12.** Fatigue test results: (a) absolute and (b) normalized S-N curves measured from the fully reversed fatigue tests, for each batch of cellular specimens. (c) Normalized fatigue strength at  $10^6$  cycles as a function of the unit cell size  $L$ . The dashed lines represent the best fitting curve (50% failure probability), while the lower and upper limit of the shaded bands indicates 10% and 90% failure probability, respectively. The black lines are the S-N curves estimated from the fatigue curve of bulk specimens and the fatigue stress concentration factor calculated from FE analyses.

crack highlighted by a white dashed line. The location of the fracture is shown in greater detail in Appendix B. Indeed, in batch A “R-“ are sharper than “R+” (Fig. 9); on the other hand, it should be also considered that the region of the fillet close to the underside of the horizontal strut is generally more irregular, leading to the identification of this area as a weak spot of the lattice.

The comparison of the S-N curve for batch B (printed horizontally) with the other batches shows that the printing direction of the struts plays a key role in dictating the fatigue behavior of lattice materials

(Fig. 12a). Batch B performs significantly worse than the batches printed vertically, regardless of the sharpness of the fillet. Remarkably, in batch B failure occurs always far from the junction, roughly in the central part of the strut (Fig. 13B and, in greater detail, Fig. B2 in the Appendix). The most likely explanation is that in batch B the struts aligned with the load are printed in the printing plane and hence they are considerably more irregular than those normal to the printing plane (Fig. 7A). In other words, if the main load-bearing role is undertaken by struts printed at small angles to the printing direction, then the junction

**Table 5**  
Comparison of the  $K_f^*$  at  $10^6$  cycles measured experimentally and calculated via FE simulations for all the batches and the specimens studied in [23].

	A	B	D	E	[23]HIPed	[23]stress-relieved
Experimental $K_f^*$	86	442	149	84	188	115
FE(nominal geometry) $K_f^*$	63	63	$\infty^{(2)}$	63	65	65
FE(as-built geometry) $K_f^*$	75	$\infty^{(1)}$	91	58	76	–
$L$ (mm)	4	4	4	3	1.5	1.5

<sup>(1)</sup> This value was not calculated because the specimens of batch B did not fail at the strut junction.

<sup>(2)</sup> Sharp junction.

is the weakest link of the lattice. On the other hand, if the main load-bearing role is undertaken by struts oriented at small angles to the printing plane, then the strut itself becomes the weakest link. Moreover, while in the case of batches A, D and E one strut fails first (on the outer annulus of the specimen) and then the fracture propagates to the neighboring ones, in batch B cracks nucleate simultaneously in several struts distributed randomly in the specimen, leading to a diffuse damage of the structure. Finally, we note that the dispersion of cycles to failure of batches A and E is higher than the others. In other words, for the same value of the load a wide range of fatigue lives is observed. The cause can be attributed to the superior morphology of batch A (wider fillets and more uniform struts) that is thus more sensitive to the presence of local geometrical defects.

Normalizing the S-N curves by the 0.2% offset strength has some interesting implications. The normalized curves (Fig. 12b) show a nearly perfect overlap for batches A, D and E while the curve for batch B is significantly lower. These results suggest that the fillet radius has a similar effect on the fatigue strength and the monotonic strength for this lattice topology: the lack of fillets increases the stress concentration and decreases the joint stiffness. As observed in other works [58,59], normalized curves for unit cells of different size but with identical topology (as batches A and E), indeed overlap. On the other hand, batch B shows that the geometrical irregularities of the horizontal struts decrease fatigue performance more than monotonic strength. In Fig. 12b also the fatigue strength at  $10^6$  cycles for cubic lattices studied in a previous work [23] is shown, together with standard deviation. These lattices have a unit cell size of 1.5 mm and were printed at  $45^\circ$  to the printing plane, i.e. the load bearing struts are inclined of  $45^\circ$  to the printing plane. These data suggest that struts printed at  $45^\circ$  perform at an intermediate level between the struts printed vertically and those

printed horizontally.

The effect of the value of the nominal geometrical parameter of the unit cell ( $L$ ,  $t_0$ , and  $R$ ) can be investigated by plotting the normalized fatigue resistance of the lattice at  $10^6$  cycles against the unit cell size  $L$  (which is related to the values of the other geometrical parameters  $t_0$  and  $R$ ). This is shown in Fig. 12c and it can be observed that by decreasing the unit cell size the resistance is constant until around 3 mm, then it drops significantly (by a factor of about 2). This result can be interpreted as an indication of the current limitation of L-PBF technology: fatigue resistant lattices can be manufactured with unit cell size down to roughly 3 mm, then the resistance drops due to manufacturing induced defects. A more precise identification of such manufacturability threshold would require more experimental tests, nevertheless it can be argued this to be located between 1.5 and 3 mm unit cell side.

Fracture surfaces (Fig. 14) show that fatigue cracks always nucleate on the surface of the struts, where the highest stresses are expected to emerge from the presence of notches. On the other hand, internal pores are observed, but their effect appears to be less detrimental than that of the surface.

It is interesting at this point to compare the experimental S-N curves with those predicted from the FE analyses based on the geometry of the unit cell and the fatigue curves of the bulk material. Clearly, there is a considerable simplification in assuming that the material properties of bulk specimens are the same as those of the base material of the lattice and, to an even greater degree, in assuming that the stress concentration factor calculated from one idealized unit cell (even if with the geometrical parameters measured from the as-built lattices) is realistic for a lattice. The estimated S-N curves (shown in Fig. 12a as black lines) are thus obtained by multiplying the fatigue notch factors calculated from the FE simulations on the nominal and on the as-built geometries of batches A and D by the S-N curve of bulk Ti-6Al-4 V (Fig. 15). The fatigue curve predicted from the nominal geometry overestimates the strength of the batch A by 33% at  $10^7$  cycles, while that predicted from the as-built geometry of batch A by only 19%. The overall low error underpins the previous observation that the fatigue behavior of this lattice is controlled by the junction geometry. The curve for  $K_f^* = 91$  is obtained with the as-built parameters of batch D, but it considerably overestimates the experimental results, suggesting that likely the notches on the underside of the horizontal struts are considerably more severe than those measured from the images. Nevertheless, it can be observed that above  $10^6$  cycles, the experimental curves are parallel to each other and quite similar to that predicted from a simplified geometry. In future work, a more accurate study of the fatigue behavior of the strut junctions will be carried out by reconstructing the stress distribution at the junctions via FE simulations based on CT scans. Finally, we emphasize that even after heat treatment there can be considerable

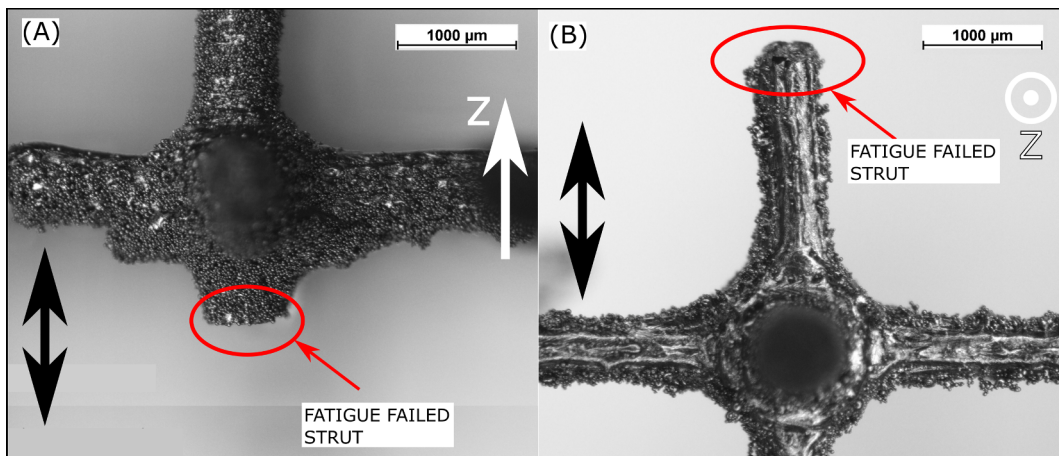


**Fig. 13.** Struts failed by fatigue: struts printed vertically fail at the junction due to the stress concentration effect of the fillet (A) while struts printed horizontally fail due to their intrinsic irregularities (B). The black double arrows indicate the loading direction while the white arrows indicate the printing direction.

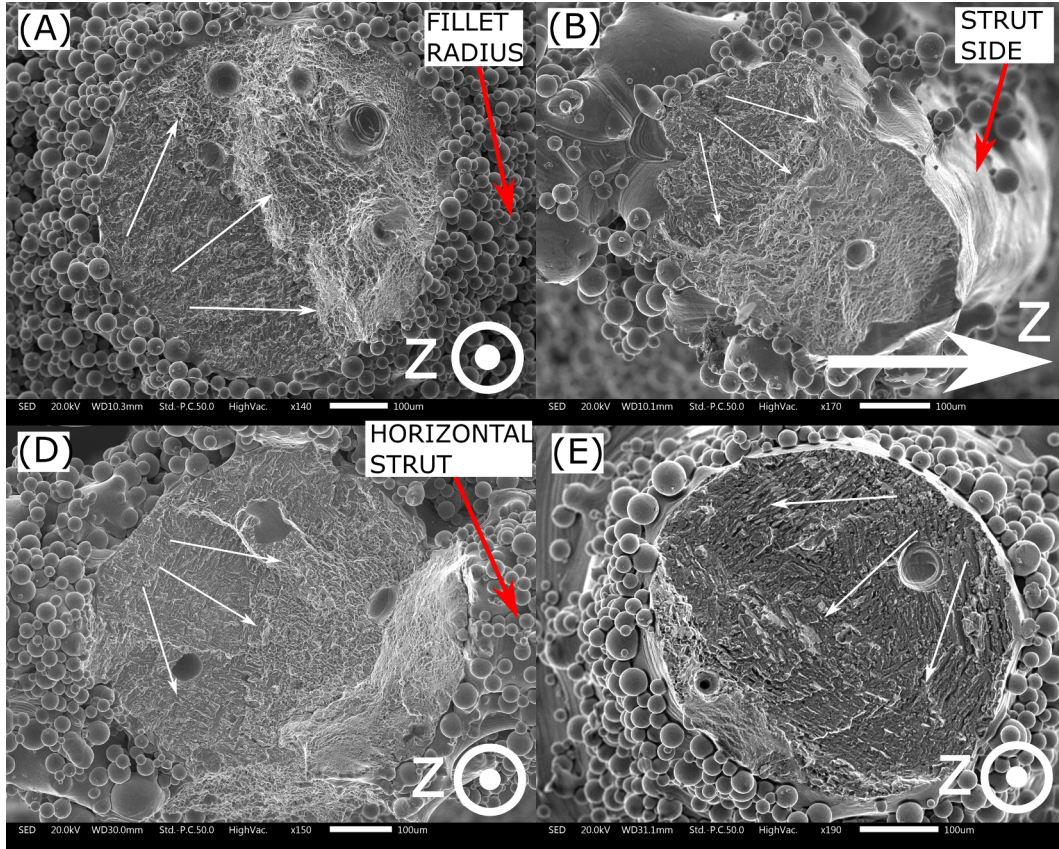


**Fig. 14.** SEM images of struts parallel to the loading direction failed by fatigue crack propagation taken on a specimen coming from batches (A), (B), (D) and (E). The small white arrows roughly indicate the direction of crack propagation from the nucleation site. Note that the cracks nucleate always on the surface, despite the presence of pores in the section.

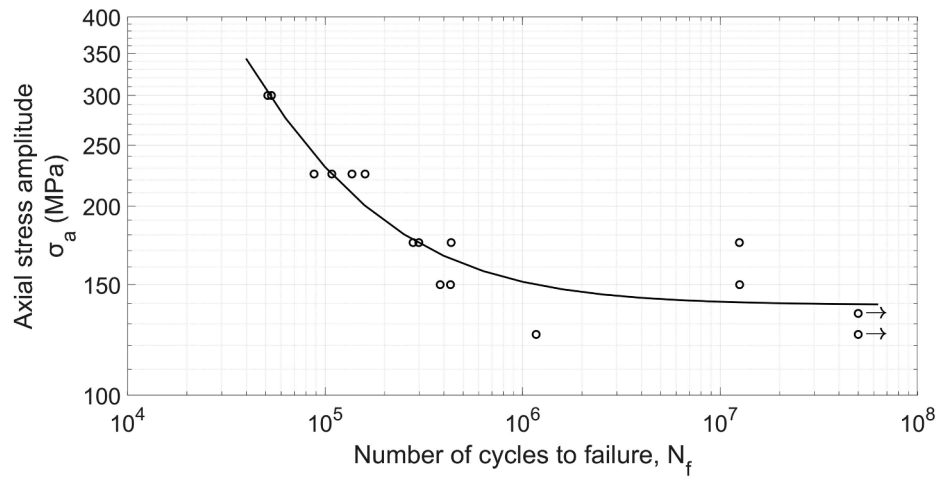


**Fig. 15.** Fatigue curve of bulk specimens.

tensile residual stresses that affect fatigue life [23].

The fatigue strength at  $10^7$  cycles from the fitted S-N curves was used to calculate  $K_f^*$  for each batch of cellular specimens (Table 5). Batches A and E show the lowest fatigue notch factor, considerably lower than a value previously measured [23], thereby showing that the up-scale strategy improves the quality of the junction geometry. The experimental results are compared with the  $K_f^*$  calculated using the stress concentration factor at the strut junctions obtained from the FE simulations as described previously (apart from the FE simulations for the HIPed specimens, which were carried out on tomography results [23]).

### 3. Conclusions

This work has investigated the fatigue response of Ti-6Al-4 V regular cubic lattices 3D printed via L-PBF at given printing directions and for prescribed morphological characteristics of the samples. In particular, the focus has been on the role of the width of the fillet radius at the strut junctions and the orientation of the struts to the printing direction in determining the S-N curves and the fatigue failure behavior. It was observed that the fatigue resistance of the lattice was markedly increased by adding round fillets between the struts at the joints. The results showed that the printing direction affects the morphology of the



struts both in terms of random surface irregularities and a systematic deviation in thickness (as-built/as-designed mismatch): the smaller the angle between the strut and the build plane, the stronger these effects are. Indeed, by appropriately orienting the structure during printing, the fatigue properties can be greatly improved.

The results of this work lead to the following conclusions:

- The orientation of the struts to the printing direction strongly affects the S-N curves and the fatigue failure behavior. In lattices with the main load bearing struts printed normally to the printing plane, cracks nucleate in the region close to the junction of the weakest strut of the lattice and then propagate to the neighboring struts. In lattices with the main load bearing struts printed parallel to the printing plane, cracks nucleate concurrently in several struts far from the filleted junctions causing diffuse damage in the structure.
- The fillet radii have been rather accurately reproduced by L-PBF, and regular shape fillets have been also obtained for the smallest nominal radius considered (200  $\mu\text{m}$ ). The scatter of the data is quite high, warning the designer on the fact that considerably sharp junctions can be found, due to local irregularities in the accumulation of parasitic mass or lack of melting. The radius on the underside of the struts (with respect to the printing direction) is consistently smaller than the fillet radius in other locations, constituting a weak

spot for fatigue. In the lattices printed vertically, failure always occurred at these locations. Nevertheless, providing the strut junctions with round fillets remarkably improves fatigue strength.

- The normalization of the S-N curves by the 0.2% offset stress showed that the printing direction affects to different degrees the fatigue and the monotonic properties. The specimens with the main load bearing struts printed parallel to the build plane show a remarkable decrease in fatigue strength while the monotonic strength is not similarly compromised.
- Upscaling the unit cell size of the lattices was shown to improve the fatigue performance due to an overall lower effect of manufacturing defects compared to lattices of a smaller scale.

## Declaration of Competing Interest

The authors declared that there is no conflict of interest.

## Acknowledgements

This research did not receive any specific grant from funding agencies in the public, commercial, or not-for-profit sectors.

## Appendix A

**Table A1**

Nominal and as-built cross-section parameters (see parameters definition in Fig. 8).

Batch	CAD $t_0(\mu\text{m})$	As-built strut cross-section parameters								
		$t_z^{ab}$			$t_{xy,z}^{ab}$			$t_{xy,xy}^{ab}$		
		$\mu(\mu\text{m})$	$\sigma(\mu\text{m})$	Dev. from CAD(%)	$\mu(\mu\text{m})$	$\sigma(\mu\text{m})$	Dev. from CAD(%)	$\mu(\mu\text{m})$	$\sigma(\mu\text{m})$	Dev. from CAD(%)
A	670	693	27	3.4	769	97	14.8	587	45	-12.4
B	670	705	27	5.2	759	115	13.3	590	58	-11.9
D	670	698	28	4.2	811	118	21.0	575	48	-14.2
E	500	527	28	5.4	524	88	4.8	450	53	-10.0

**Table A2**

Nominal and as-built strut junction parameters (see parameters definition in Fig. 9).

Batch	CAD $R(\mu\text{m})$	As-built struts junction parameters								
		$R_+$			$R_-$			$R_{lat}$		
		$\mu(\mu\text{m})$	$\sigma(\mu\text{m})$	Dev. from CAD (%)	$\mu(\mu\text{m})$	$\sigma(\mu\text{m})$	Dev. from CAD (%)	$\mu(\mu\text{m})$	$\sigma(\mu\text{m})$	Dev. from CAD (%)
A	600	586	103	-2.3	318	148	-47.0	778	130	29.7
B	600	576	168	-4.0	383	172	-36.2	824	219	37.3
D	600	90	25	-85.0	102	33	-83.0	176	98	-70.7
E	450	442	126	-1.8	445	180	-1.1	789	113	75.3

## Appendix B

In this Appendix, more details of the fracture surfaces of the specimens are provided. We created one figure for each batch (Figs. B1–B4) in which we reconstructed, pasting together several pictures obtained with the SEM, a small part of the fractured section of one specimen. The region of the specimen where the struts failed by fatigue is highlighted by a white dashed square in the picture of the entire specimen. The same region is shown magnified in the collage of SEM pictures where the red arrows indicate the propagation of the fatigue crack front on the specimen cross-section. The fracture surfaces of the struts are further magnified to show both the fracture surface and the location of the fracture relative to the junction. The fatigue tests were stopped after a 1 Hz decrease in frequency (4–5 broken struts) and then the two parts of the specimen were separated via a monotonic tensile load. It is thus possible to identify the nucleation site of the fatigue crack, given that the fatigue fracture surfaces are smooth, while the fracture surface of the struts failed by monotonic load show the typical dimples. The magnified fracture surfaces of the struts failed by fatigue are enclosed in red dashed rectangles and the white arrows indicate the fatigue crack propagation direction.



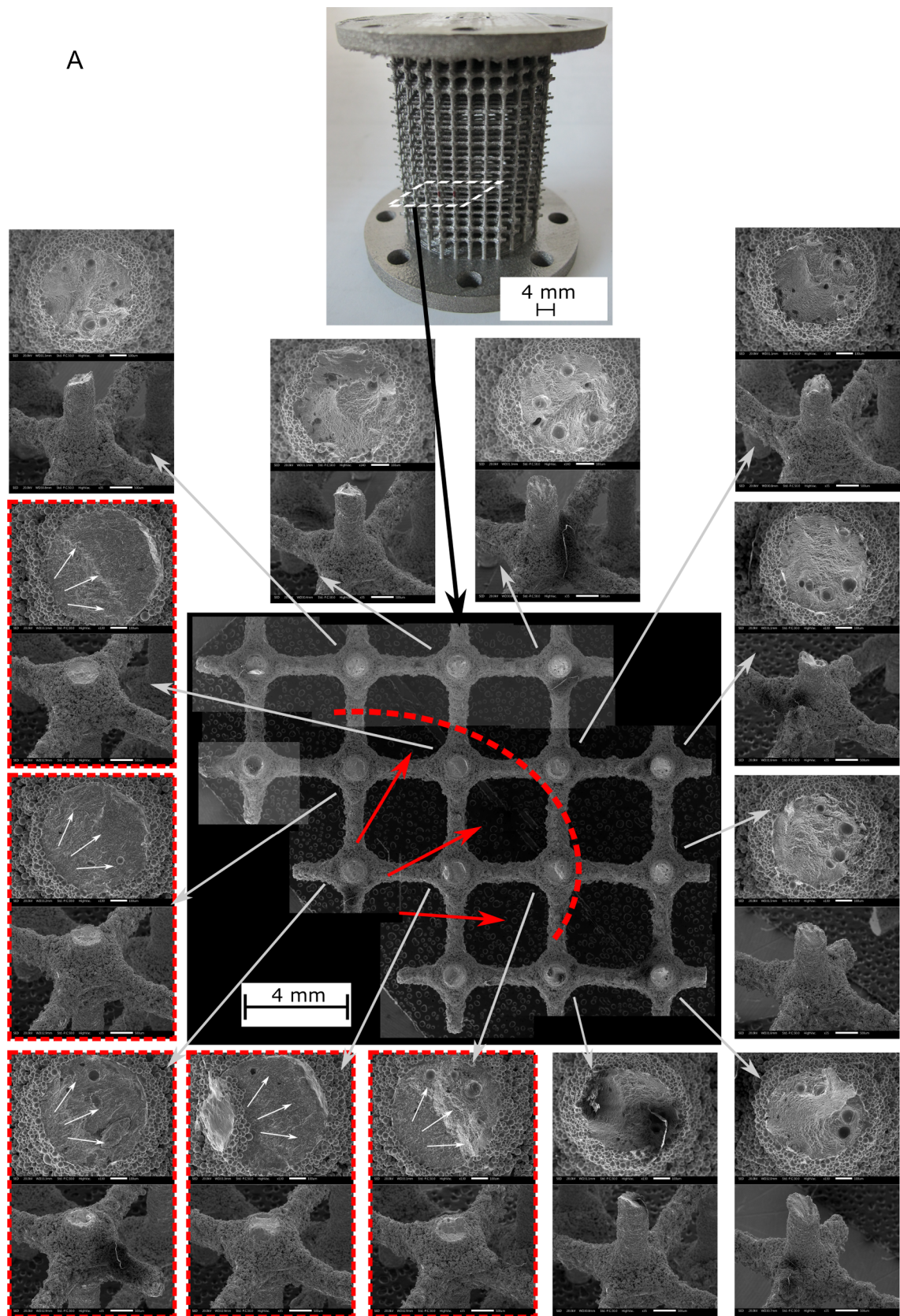


Fig. B1. Fracture analysis of one specimen of batch A.

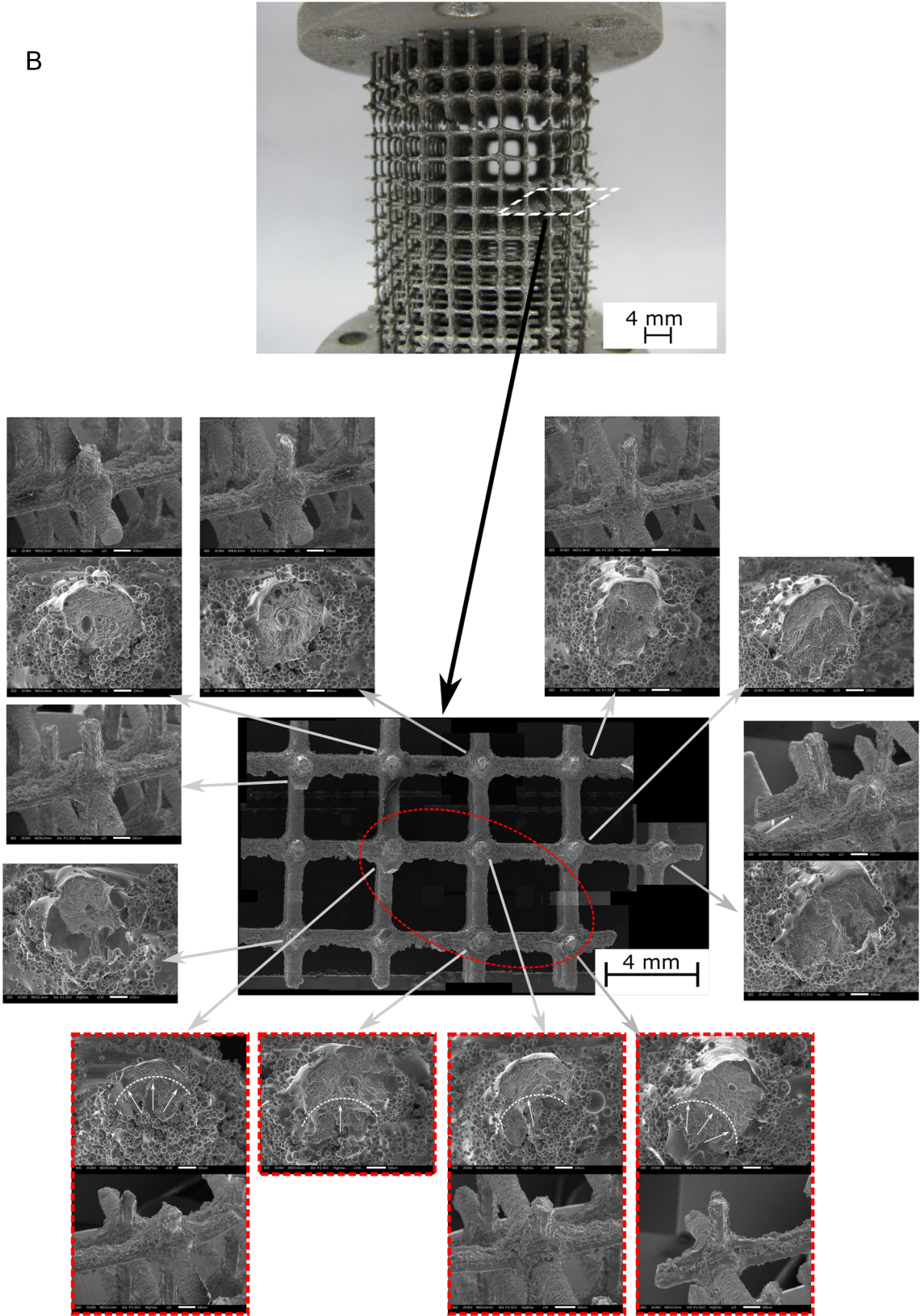


Fig. B2. Fracture analysis of one specimen of batch B.



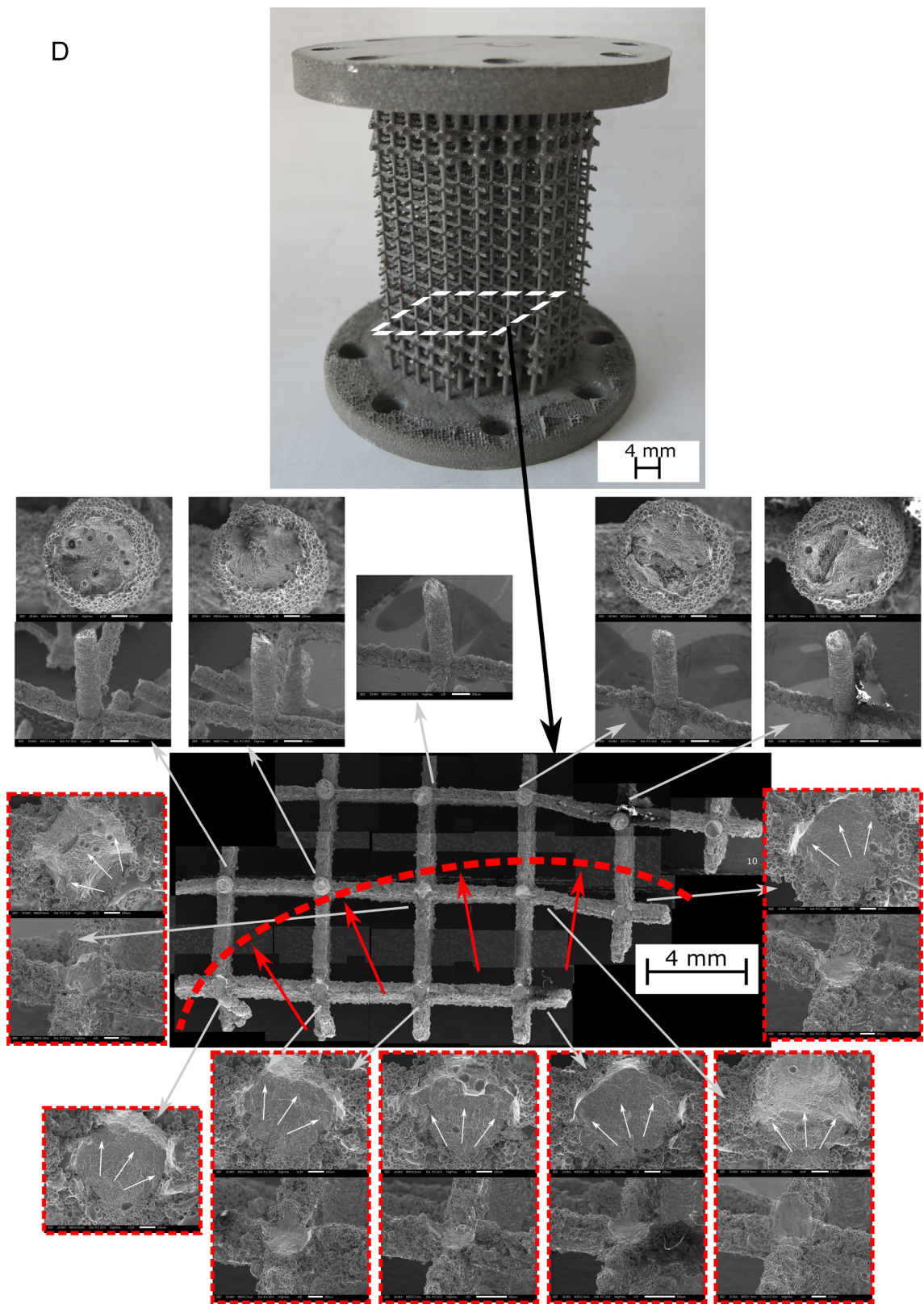


Fig. B3. Fracture analysis of one specimen of batch D.

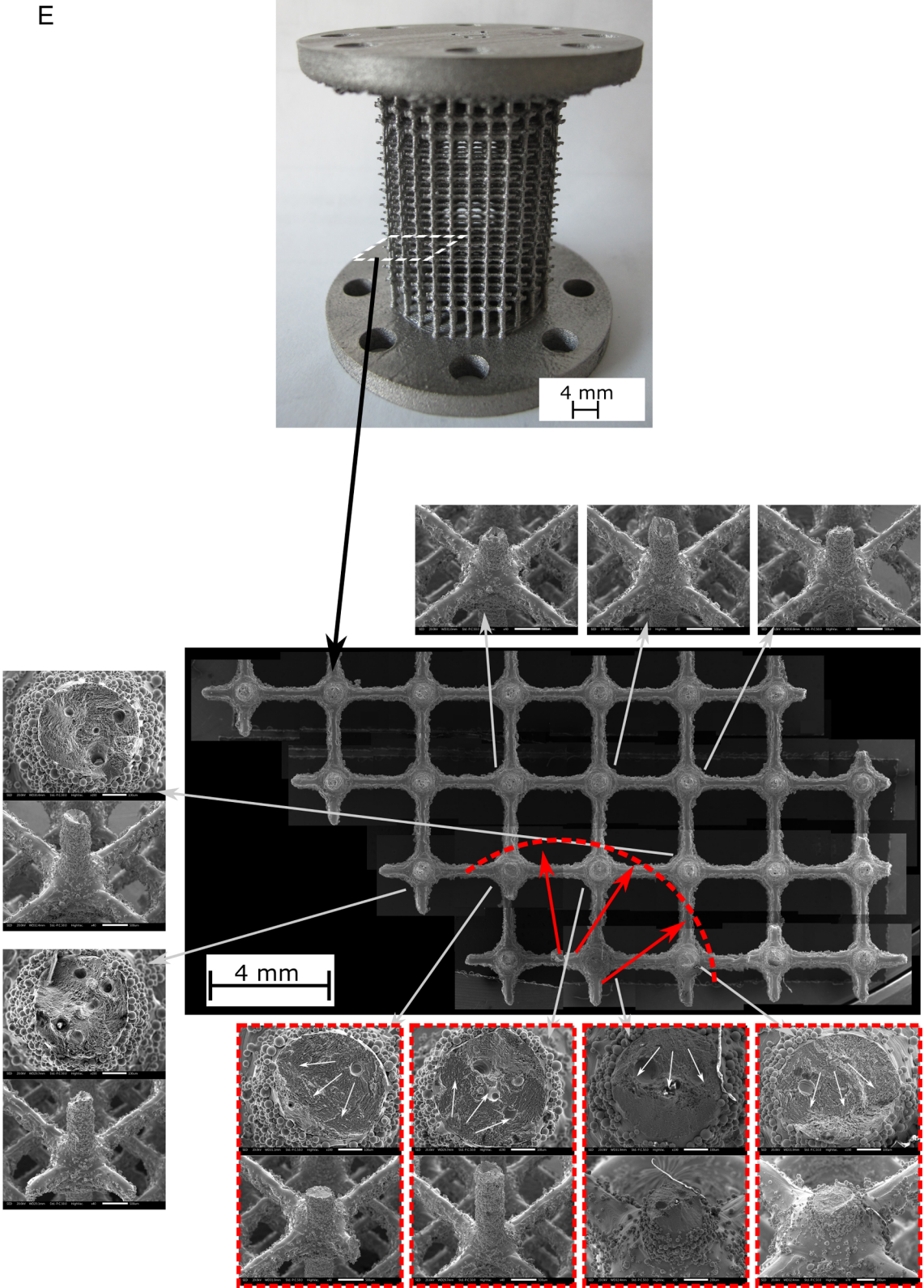


Fig. B4. Fracture analysis of one specimen of batch E.



## References

- [1] Gibson LJ, Ashby MF, Harley BA. *Cellular materials in nature and medicine*. Cambridge University Press; 2010.
- [2] Ashby MF. The properties of foams and lattices. *Philos Trans R Soc A Math Phys Eng Sci* 2006;364:15–30. <https://doi.org/10.1098/rsta.2005.1678>.
- [3] Gibson LJ, Ashby MF. *Cellular Solids - Structure and Properties*. 2 ed. Cambridge University Press; 1999.
- [4] Fleck NA, Deshpande VS, Ashby MF. Micro-architected materials: Past, present and future. *Proc R Soc A Math Phys Eng Sci* 2010;466:2495–516. <https://doi.org/10.1098/rspa.2010.0215>.
- [5] Maconachie T, Leary M, Lozanovski B, Zhang X, Qian M, Faruque O, et al. Materials & Design SLM lattice structures : Properties, performance, applications and challenges. *Mater Des* 2019;183:108137. <https://doi.org/10.1016/j.matdes.2019.108137>.
- [6] Rashed MG, Ashraf M, Mines RAW, Hazell PJ. Metallic microlattice materials: A current state of the art on manufacturing, mechanical properties and applications. *Mater Des* 2016;95:518–33. <https://doi.org/10.1016/j.matdes.2016.01.146>.
- [7] Sumner DR. Long-term implant fixation and stress-shielding in total hip replacement. *J Biomech* 2015;48:797–800. <https://doi.org/10.1016/j.jbiomech.2014.12.021>.
- [8] Murr LE, Gaytan SM, Medina F, Lopez H, Martinez E, Machado BI, et al. Next-generation biomedical implants using additive manufacturing of complex cellular and functional mesh arrays. *Philos Trans R Soc A Math Phys Eng Sci* 2010;368:1999–2032. <https://doi.org/10.1098/rsta.2010.0010>.
- [9] Tan XP, Tan YJ, Chow CSL, Tor SB, Yeong WY. Metallic powder-bed based 3D printing of cellular scaffolds for orthopaedic implants: A state-of-the-art review on manufacturing, topological design, mechanical properties and biocompatibility. *Mater Sci Eng C* 2017;76:1328–43. <https://doi.org/10.1016/j.msec.2017.02.094>.
- [10] Arabnejad S, Burnett Johnston R, Pura JA, Singh B, Tanzer M, Pasini D. High-strength porous biomaterials for bone replacement: A strategy to assess the interplay between cell morphology, mechanical properties, bone ingrowth and manufacturing constraints. *Acta Biomater* 2016;30:345–56. <https://doi.org/10.1016/j.actbio.2015.10.048>.
- [11] Sing SL, An J, Yeong WY, Wiria FE. Laser and electron-beam powder-bed additive manufacturing of metallic implants: A review on processes, materials and designs. *J Orthop Res* 2016;34:369–85. <https://doi.org/10.1002/jor.23075>.
- [12] Zadpoor AA. Design for additive bio-manufacturing : from patient-specific medical devices to rationally designed meta-biomaterials. *Int J Mol Sci* 2017;18:1–18. <https://doi.org/10.3390/ijms18081607>.
- [13] Ian Gibson · David Rosen Brent Stucker. *Additive Manufacturing Technologies*. 2015. doi:10.1520/F2792-12A.2.
- [14] Murr LE, Gaytan SM, Ramirez DA, Martinez E, Hernandez J, Amato KN, et al. Metal fabrication by additive manufacturing using laser and electron beam melting technologies. *J Mater Sci Technol* 2012;28:1–14. [https://doi.org/10.1016/S1005-0302\(12\)60016-4](https://doi.org/10.1016/S1005-0302(12)60016-4).
- [15] Arabnejad S, Johnston B, Tanzer M, Pasini D. Fully Porous 3D Printed Titanium Femoral Stem to Reduce Stress-Shielding Following Total Hip Arthroplasty 2016:29–31. doi:10.1002/jor.23445.
- [16] Pasini D, Guest JK. Imperfect architected materials: Mechanics and topology optimization. *MRS Bull* 2019;44:766–72. <https://doi.org/10.1557/mrs.2019.231>.
- [17] Dong G, Tang Y, Zhao YF. A survey of modeling of lattice structures fabricated by additive manufacturing. *J Mech Des* 2017;139:1–13. <https://doi.org/10.1115/1.4037305>.
- [18] Zadpoor AA. Mechanics of additively manufactured biomaterials. *J Mech Behav Biomed Mater* 2017;70:1–6. <https://doi.org/10.1016/j.jmbbm.2017.03.018>.
- [19] Weißmann V, Drescher P, Bader R, Seitz H, Hansmann H, Laufer N. Comparison of single Ti6Al4V struts made using selective laser melting and electron beam melting subject to part orientation. *Metals (Basel)* 2017;7:91. <https://doi.org/10.3390/met7030091>.
- [20] Weißmann V, Bader R, Hansmann H, Laufer N. Influence of the structural orientation on the mechanical properties of selective laser melted Ti6Al4V open-porous scaffolds. *Mater Des* 2016;95:188–97. <https://doi.org/10.1016/j.matdes.2016.01.095>.
- [21] Wauthle R, Vrancken B, Beynaerts B, Jorissen K, Schrooten J, Kruth JP, et al. Effects of build orientation and heat treatment on the microstructure and mechanical properties of selective laser melted Ti6Al4V lattice structures. *Addit Manuf* 2015;5:77–84. <https://doi.org/10.1016/j.addma.2014.12.008>.
- [22] Zhang B, Li Y, Bai Q. Defect formation mechanisms in selective laser melting: a review. *Chinese J Mech Eng (English Ed)* 2017;30:515–27. <https://doi.org/10.1007/s10033-017-0121-5>.
- [23] Dallago M, Winiarski B, Zanini F, Carmignato S, Benedetti M. On the effect of geometrical imperfections and defects on the fatigue strength of cellular lattice structures additively manufactured via Selective Laser Melting. *Int J Fatigue* 2019;124:348–60. <https://doi.org/10.1016/j.ijfatigue.2019.03.019>.
- [24] Herzog D, Seyda V, Wycisk E, Emmelmann C. Additive manufacturing of metals. *Acta Mater* 2016;117:371–92. <https://doi.org/10.1016/j.actamat.2016.07.019>.
- [25] Melancon D, Bagheri ZS, Johnston RB, Liu L, Tanzer M, Pasini D. Mechanical characterization of structurally porous biomaterials built via additive manufacturing: experiments, predictive models, and design maps for load-bearing bone replacement implants. *Acta Biomater* 2017;63:350–68. <https://doi.org/10.1016/j.actbio.2017.09.013>.
- [26] Takano N, Takizawa H, Wen P, Odaka K, Matsunaga S, Abe S. Stochastic prediction of apparent compressive stiffness of selective laser sintered lattice structure with geometrical imperfection and uncertainty in material property. *Int J Mech Sci* 2017;134:347–56. <https://doi.org/10.1016/j.ijmecsci.2017.08.060>.
- [27] Leary M. Design of titanium implants for additive manufacturing. In: Froes F, Qian M, editors. *Titan. Med. Dent. Appl.*, Woodhead Publishing; 2018, p. 203–24. doi:10.1016/b978-0-12-812456-7.00009-3.
- [28] Mazur M, Leary M, McMillan M, Sun S, Shidid D, Brandt M. Mechanical properties of Ti6Al4V and AlSi12Mg lattice structures manufactured by Selective Laser Melting (SLM). In: Brandt M, editor. *Laser Addit. Manuf. Mater. Des. Technol. Appl.*, Woodhead Publishing; 2017, p. 119–61. doi:10.1016/B978-0-08-100433-3.00005-1.
- [29] Bagheri ZS, Melancon D, Liu L, Johnston RB, Pasini D. Compensation strategy to reduce geometry and mechanics mismatches in porous biomaterials built with selective laser melting. *J Mech Behav Biomed Mater* 2017;70:17–27. <https://doi.org/10.1016/j.jmbbm.2016.04.041>.
- [30] Liu L, Kamm P, García-Moreno F, Banhart J, Pasini D. Elastic and failure response of imperfect three-dimensional metallic lattices: the role of geometric defects induced by selective laser melting. *J Mech Phys Solids* 2017;107:160–84. <https://doi.org/10.1016/j.jmps.2017.07.003>.
- [31] Dallago M, Raghavendra S, Luchin V, Zappini G, Pasini D, Benedetti M. Geometric assessment of lattice materials built via selective laser melting. *Mater TodayProc* 2019;7:353–61. <https://doi.org/10.1016/j.matpr.2018.11.096>.
- [32] Qiu C, Yue S, Adkins NJE, Ward M, Hassanin H, Lee PD, et al. Influence of processing conditions on strut structure and compressive properties of cellular lattice structures fabricated by selective laser melting. *Mater Sci Eng A* 2015;628:188–97. <https://doi.org/10.1016/j.msea.2015.01.031>.
- [33] Sing SL, Wiria FE, Yeong WY. Selective laser melting of lattice structures: A statistical approach to manufacturability and mechanical behavior. *Robot Comput Integr Manuf* 2018;49:170–80. <https://doi.org/10.1016/j.rcim.2017.06.006>.
- [34] Pyka G, Kerckhofs G, Papanthiou I, Speirs M, Schrooten J, Wevers M. Surface roughness and morphology customization of additive manufactured open porous Ti6Al4V structures. *Materials (Basel)* 2013;6:4737–57. <https://doi.org/10.3390/ma6104737>.
- [35] Kranz J, Herzog D, Emmelmann C. Design guidelines for laser additive manufacturing of lightweight structures in TiAl6V4. *J Laser Appl* 2015;27:S14001. <https://doi.org/10.2351/1.4885235>.
- [36] Calignano F. Design optimization of supports for overhanging structures in aluminum and titanium alloys by selective laser melting. *J Mater* 2014;64:203–13. <https://doi.org/10.1016/j.matdes.2014.07.043>.
- [37] Kessler J, Balc N, Gebhardt A, Abbas K. Basic design rules of unit cells for additive manufactured lattice structures. *MATEC Web Conf* 2017;137. <https://doi.org/10.1007/BF01171954>.
- [38] Yan C, Hao L, Hussein A, Young P, Raymond D. Advanced lightweight 316L stainless steel cellular lattice structures fabricated via selective laser melting. *Mater Des* 2014;55:533–41. <https://doi.org/10.1016/j.matdes.2013.10.027>.
- [39] Zhu Z, Anwer N, Mathieu L. Deviation modeling and shape transformation in design for additive manufacturing. *Procedia CIRP* 2017;60:211–6. <https://doi.org/10.1016/j.procir.2017.01.023>.
- [40] Campoli G, Borleffs MS, Amin Yavari S, Wauthle R, Weinans H, Zadpoor AA. Mechanical properties of open-cell metallic biomaterials manufactured using additive manufacturing. *Mater Des* 2013;49:957–65. <https://doi.org/10.1016/j.matdes.2013.01.071>.
- [41] Torries B, Imandoust A, Beretta S, Shao S, Shamsaei N. Overview on Microstructure and Defect-Sensitive Fatigue Modeling of Additively Manufactured Materials. *JOM* 2018;70:1853–62. <https://doi.org/10.1007/s11837-018-2987-9>.
- [42] Takano N, Fukasawa K, Nishiyabu K. Structural strength prediction for porous titanium based on micro-stress concentration by micro-CT image-based multiscale simulation. *Int J Mech Sci* 2010;52:229–35. <https://doi.org/10.1016/j.ijmecsci.2009.09.013>.
- [43] Lozanovski B, Leary M, Tran P, Shidid D, Qian M, Choong P, et al. Computational modelling of strut defects in SLM manufactured lattice structures. *Mater Des* 2019;171:107671. <https://doi.org/10.1016/j.matdes.2019.107671>.
- [44] Dowling NE. *Mechanical Behavior of Materials*. Pearson Education: Fourth ed.; 2013.
- [45] Vayssette B, Saintier N, Brugger C, Elmay M, Pessard E. Surface roughness of Ti-6Al-4V parts obtained by SLM and EBM: effect on the high cycle fatigue life. *Procedia Eng* 2018;213:89–97. <https://doi.org/10.1016/j.proeng.2018.02.010>.
- [46] Fotovvati B, Namdari N, Dehghanghadikolaei A. Fatigue performance of selective laser melted Ti6Al4V components: State of the art. *Mater Res Express* 2019;6. <https://doi.org/10.1088/2053-1591/ae10e>.
- [47] Ren D, Li S, Wang H, Hou W, Hao Y, Jin W, et al. Fatigue behavior of Ti-6Al-4V cellular structures fabricated by additive manufacturing technique. *J Mater Sci* 2019;35:285–94.
- [48] Dallago M, Fontanari V, Torresani E, Leoni M, Pederzoli C, Potrich C, et al. Fatigue and biological properties of Ti-6Al-4V ELI cellular structures with variously arranged cubic cells made by selective laser melting. *J Mech Behav Biomed Mater* 2018;78. <https://doi.org/10.1016/j.jmbbm.2017.11.044>.
- [49] Boniotti L, Beretta S, Patriarca L, Rigoni L, Foletti S. Experimental and numerical investigation on compressive fatigue strength of lattice structures of AlSi7Mg manufactured by SLM. *Int J Fatigue* 2019;128:105181. <https://doi.org/10.1016/j.ijfatigue.2019.06.041>.
- [50] Du Plessis A, Kouprianoff DP, Yadroitsev I, Yadroitsev I. Mechanical properties and in situ deformation imaging of microlattices manufactured by laser based powder bed fusion. *Materials (Basel)* 2018;11. <https://doi.org/10.3390/ma11091663>.
- [51] Lohmuller P, Favre J, Piotrowski B, Kenzari S, Laheurte P. Stress concentration and mechanical strength of cubic lattice architectures. *Materials (Basel)* 2018;11:1–12.

- <https://doi.org/10.3390/ma11071146>.
- [52] Benedetti M, Fontanari V, Bandini M, Zanini F, Carmignato S. Low- and high-cycle fatigue resistance of Ti-6Al-4V ELI additively manufactured via selective laser melting: Mean stress and defect sensitivity. *Int J Fatigue* 2018;107:96–109. <https://doi.org/10.1016/j.ijfatigue.2017.10.021>.
- [53] Niinomi M. Mechanical properties of biomedical titanium alloys. *Mater Sci Eng A* 1998;243:231–6. [https://doi.org/10.1016/S0921-5093\(97\)00806-X](https://doi.org/10.1016/S0921-5093(97)00806-X).
- [54] Benedetti M, Santus C. Notch fatigue and crack growth resistance of Ti-6Al-4V ELI additively manufactured via selective laser melting: A critical distance approach to defect sensitivity. *Int J Fatigue* 2019;121:281–92. <https://doi.org/10.1016/J.IJFATIGUE.2018.12.020>.
- [55] Leuders S, Thöne M, Riemer A, Niendorf T, Tröster T, Richard HA, et al. On the mechanical behaviour of titanium alloy TiAl6V4 manufactured by selective laser melting: Fatigue resistance and crack growth performance. *Int J Fatigue* 2013;48:300–7. <https://doi.org/10.1016/j.ijfatigue.2012.11.011>.
- [56] Rodney B, Gerhard W. *Materials Properties Handbook: Titanium Alloy*. Materials Park, OH: ASM International; 1994.
- [57] Ashby MF, Evans AG, Fleck NA, Gibson LJ, Hutchinson JW, Wadley HNG. *Metal Foams: A Design Guide*. Butterworth Heinemann 2000.
- [58] Amin Yavari S, Wauthle R, Van Der Stok J, Riemslag AC, Janssen M, Mulier M, et al. Fatigue behavior of porous biomaterials manufactured using selective laser melting. *Mater Sci Eng C* 2013;33:4849–58. <https://doi.org/10.1016/j.msec.2013.08.006>.
- [59] Amin Yavari S, Ahmadi SM, Wauthle R, Pouran B, Schrooten J, Weinans H, et al. Relationship between unit cell type and porosity and the fatigue behavior of selective laser melted meta-biomaterials. *J Mech Behav Biomed Mater* 2015;43:91–100. <https://doi.org/10.1016/j.jmbbm.2014.12.015>.